



**HAL**  
open science

## Characterization of aqueous alteration and formation of salty exposures at Ius Chasma, Mars

Kierra Wilk, Janice Bishop, Catherine Weitz, Mario Parente, Arun M. Saranathan, Yuki Itoh, Christoph Gross, Jessica Flahaut, Frank Seelos

### ► To cite this version:

Kierra Wilk, Janice Bishop, Catherine Weitz, Mario Parente, Arun M. Saranathan, et al.. Characterization of aqueous alteration and formation of salty exposures at Ius Chasma, Mars. *Icarus*, 2024, 408, pp.115800. <10.1016/j.icarus.2023.115800>. <hal-04251947>

**HAL Id: hal-04251947**

**<https://hal.science/hal-04251947v1>**

Submitted on 9 Oct 2024

HAL is a multi-disciplinary open access archive for the deposit and dissemination of scientific research documents, whether they are published or not. The documents may come from teaching and research institutions in France or abroad, or from public or private research centers.

L'archive ouverte pluridisciplinaire HAL, est destinée au dépôt et à la diffusion de documents scientifiques de niveau recherche, publiés ou non, émanant des établissements d'enseignement et de recherche français ou étrangers, des laboratoires publics ou privés.



Distributed under a Creative Commons CC BY-NC-ND 4.0 - Attribution - Non-commercial use - No Derivative Works - International License



47  
48

## 49 1. Introduction

50

51 Valles Marineris extends over ~ 4000 km along the Martian equator, exposing a wide  
52 variety of mineralogy ranging from basaltic components to sulfates and phyllosilicates. The  
53 complex canyon system (Fueten et al., 2014) formed after the accumulation of lavas that were  
54 part of the Tharsis volcanism (Tanaka, 1986; Tanaka et al., 1991) and include Noachian-aged  
55 ancestral basins (Lucchitta and Bertolini, 1990; Lucchitta et al., 1994) that were reshaped during  
56 the Hesperian to the current structure (Scott and Tanaka, 1986; Tanaka, 1986; Dohm and  
57 Tanaka, 1999; Head et al., 2001; Carr and Head, 2010) and modified with faulting and linear  
58 troughs in the Amazonian (Schultz, 1998). Water has also played an important role in shaping  
59 (Sivasankari and Arivazhagan, 2022) and creating alteration products and sediments within  
60 Valles Marineris (Gendrin et al., 2005; Chojnacki and Hynek, 2008; Murchie et al., 2009a).

61 Throughout the Valles Marineris region, light-toned layered deposits have been observed  
62 along the plateaus by the Mars Reconnaissance Orbiter (MRO) HiRISE (McEwen et al., 2007)  
63 and CRISM (S. L. Murchie et al., 2007) instruments west of Ganges Chasma, southwest of  
64 Melas Chasma, south of western Candor Chasma, northwest of Juventae Chasma, south of Ius  
65 Chasma (Weitz et al., 2010) and south of Coprates and Capri Chasmata (Le Deit et al., 2012).  
66 These light-toned layered deposits are associated with valley or channel systems, with three of  
67 the deposits (Juventae, Ius, and Ganges Chasma) having inverted channels made of light-toned  
68 beds (Weitz et al., 2010). Within the canyons of Valles Marineris, thicker mounds of light-toned  
69 layered deposits are spectrally dominated by hydrated sulfates, including monohydrated sulfates  
70 (MHS) and polyhydrated sulfates (PHS) visible at km scales in the Mars Express Observatoire  
71 pour la Mineralogie, l'Eau, les Glaces et l'Activite' (OMEGA) (Gendrin et al., 2005; Bibring et  
72 al., 2006) and MRO/CRISM data (e.g. Murchie et al., 2009a). Horizons of PHS and MHS units,  
73 sometimes alternating but frequently with PHS above MHS, have been observed in many of the  
74 chasmata across Valles Marineris and nearby including Candor Chasma (Murchie et al., 2009b;  
75 Roach et al., 2009; Fueten et al., 2014), Capri Chasma (Flahaut et al., 2010; Weitz et al., 2012),  
76 and Juventae Chasma (Bishop et al., 2009; Noel et al., 2015; Fueten et al., 2017) .

77 Orbital characterization of the unique light-toned outcrops on Mars using CRISM data  
78 indicate broader geochemical transitions from sedimentary phyllosilicate beds to evaporative,  
79 acidic, or hydrothermal environments containing sulfate minerals (e.g. Bibring et al., 2006).  
80 Several thin outcrops have been identified on Mars using a spectral "doublet" feature with two  
81 absorption bands between 2.2 – 2.3  $\mu\text{m}$  at multiple locations including Mawrth Vallis (Bishop et  
82 al., 2020), Noctis Labyrinthus (Weitz et al., 2011), Melas Chasma (Weitz et al., 2015), Coprates  
83 Catena (Weitz and Bishop, 2016), and Ius Chasma (Roach et al., 2010). The "doublet" type units  
84 at Mawrth Vallis are sandwiched in between Al-phyllosilicates and Fe/Mg-smectites in  
85 expansive clay beds and in some cases, small pockets of jarosite are observed in or adjacent to  
86 the "doublet" materials (Bishop et al., 2020). Noctis Labyrinthus, adjoined to the westernmost  
87 chasmata of Valles Marineris, is known for mineralogic diversity with outcrops containing  
88 multiple aqueous minerals (Weitz et al., 2011; Thollot et al., 2012) and also this "doublet"  
89 signature (Weitz et al., 2011). The spectral "doublet" units observed at Melas Chasma occur in  
90 smaller outcrops along the upper wall rock slopes in far western Melas adjacent to Ius Chasma  
91 (Weitz et al., 2015). This study builds on these previous orbital studies of the doublet materials

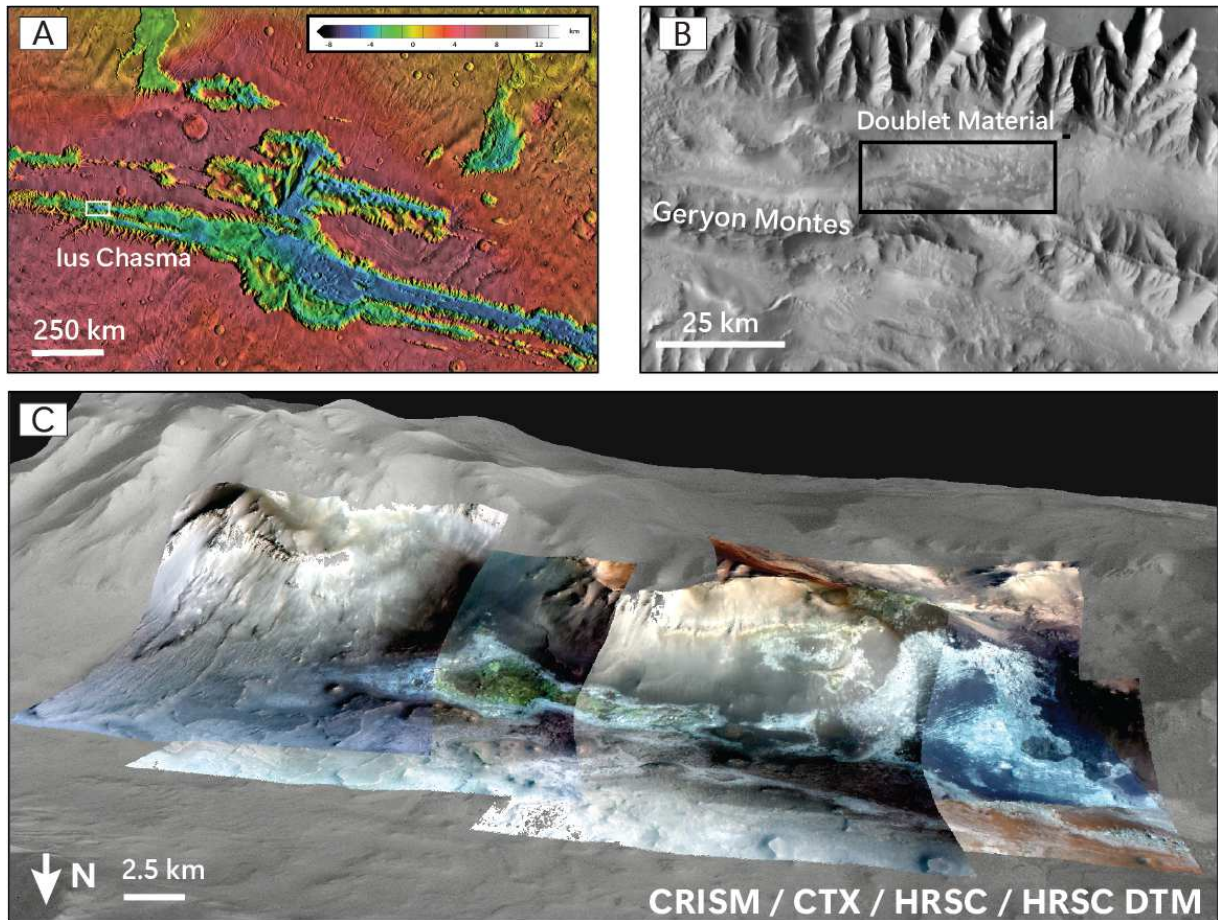
92 and spectral analyses of analog sites containing phyllosilicate-sulfate assemblages (Bishop et al.,  
93 2015, 2005)(Kaplan et al., 2016; S. Perrin et al., 2018)(Bishop et al., 2019). Here we focus on Ius  
94 Chasma (Figure 1), which contains perhaps the most intriguing “doublet” type units, as they  
95 form a continuous thin sloped layer that spans tens of kilometers.

96 Previous work (Roach et al., 2010; Kaplan et al., 2016) investigated these enigmatic  
97 “doublet” materials found in the light-toned layered deposits at Ius Chasma that span hundreds of  
98 kilometers. The “doublet” materials are emplaced on top of Fe/Mg smectites, and their origin has  
99 been interpreted as being either an acid-leached phyllosilicate from the underlying unit, or as a  
100 smectite/jarosite mixture (Roach et al., 2010). Analysis of spectral and mineralogical analogs  
101 from Rio Tinto led Kaplan et al. (2016) suggest that the “doublet” material is consistent with an  
102 Al-phyllosilicate and jarosite mixture due to the independently varying strength of the doublet  
103 feature, the similarity in the spectral doublet wavelength positions seen at both Rio Tinto and on  
104 Mars, and the wavelength positions of the spectral doublet feature being somewhat consistent  
105 with Al-OH and Fe-OH bearing minerals.

106 Itoh and Parente (2021) recently proposed a new atmospheric correction and de-noising  
107 algorithm, SUBCONV, for CRISM IR images that significantly mitigates atmospheric residuals  
108 and spurious features, clarifying surface spectral features. Furthermore, Saranathan and Parente,  
109 2021 developed novel feature extracting algorithms that allow for the isolation and mapping of  
110 unique image components using the CRISM images processed by the SUBCONV algorithm. The  
111 advancement of the improved CRISM image processing and mineral mapping techniques  
112 enables the characterization of smaller outcrops that were previously difficult to resolve.

113 The objectives of our study are to reinvestigate these intriguing spectral “doublet”  
114 outcrops near Geryon Montes in Ius Chasma through coordinated analyses of compositional  
115 information from CRISM and morphology and stratigraphy from HiRISE and the Mars Express  
116 High Resolution Stereo Camera (HRSC). Our analysis includes a high level CRISM product set,  
117 the Map-Projected Targeted Reduced Data Records (MTRDR) (Seelos et al., 2023), processed  
118 and released by the CRISM Science Operation Center, though we are primarily employing the  
119 newer SUBCONV image processing technique that offers improved clarity of CRISM images  
120 with reduced noise and improved spectral features of surface outcrops, coupled with the new  
121 feature extraction algorithm to map out spectrally distinct components in these scenes. We are  
122 using these techniques to explore the types of minerals and other components that best explain  
123 the doublet features and to assess how these intriguing deposits formed at Ius Chasma.

124



125  
 126  
 127  
 128  
 129  
 130  
 131

**Figure 1:** (A) MOLA image of Valles Marineris, including Ius Chasma. (B) THEMIS Day IR image of Ius Chasma including Geryon Montes and the bright layered materials containing the “doublet” spectral signatures. (C) HRSC DTM overlain by CTX and CRISM images of the doublet type unit on the southern wall of the northern valley of Ius Chasma.

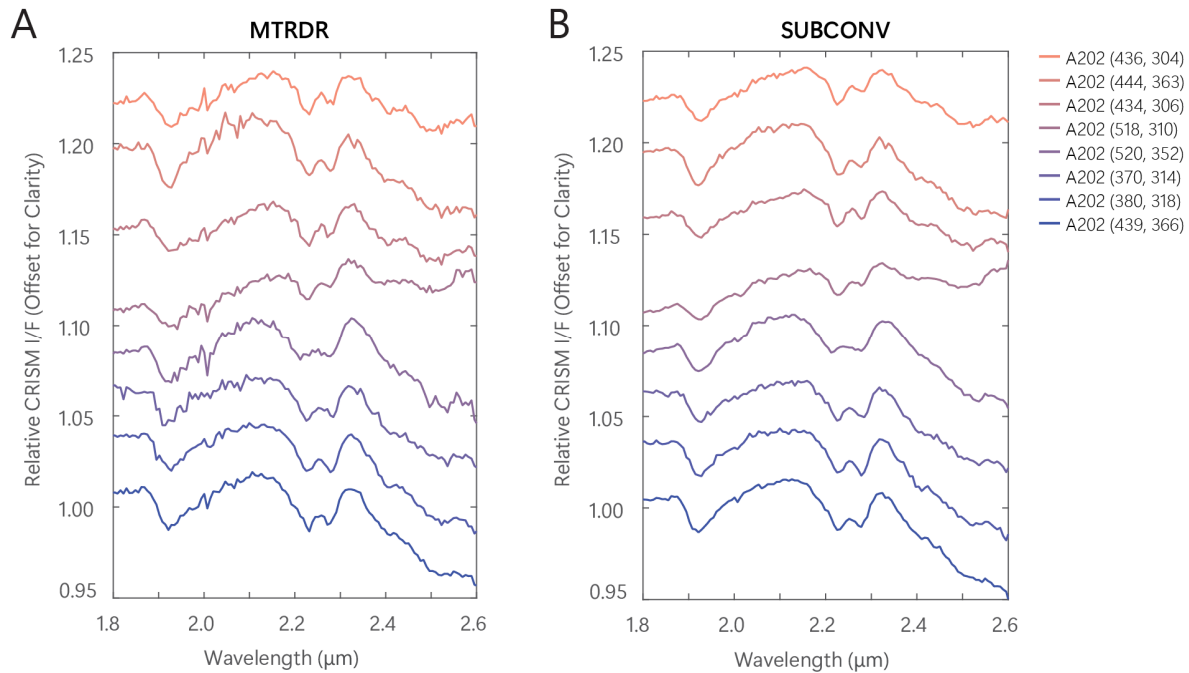
## 132 2. Methods

133  
 134  
 135  
 136  
 137  
 138  
 139  
 140  
 141  
 142  
 143  
 144  
 145

This study focuses on visible/near-infrared (VNIR) spectral image cubes acquired by the CRISM instrument in the Full Resolution Targeted (FRT) observation mode that nominally achieves the spatial resolution of 18 m/pixel. We made use of the I/F image cubes of the MTRDR products (Seelos et al., 2023) that were already photometrically and atmospherically corrected and map projected. Some of the remaining residuals in the I/F spectra in the MTRDR product are mitigated by ratioing spectra from areas of interest to spectrally neutral sites in the image. Spectral parameters (Viviano et al., 2014) were further used to identify and map individual mineral units in complex outcrops in CRISM scenes. ArcGIS software was then used to overlay CRISM maps of specific minerals (e.g., Bishop et al., 2020) on imagery collected by HiRISE, the Context (CTX) camera onboard MRO and HRSC digital terrain models (DTM).

For this study we are also using CRISM images prepared with the new SUBCONV algorithm developed by Itoh and Parente (2021) for simultaneous atmospheric correction and

146 denoising processed using the older TRDR-equivalent I/F data produced by our own  
 147 implementation of the TRDR version 3 calibration pipeline excluding bad-pixel interpolation and  
 148 TRR3 filtering. Images processed using this new method are free of most of the residual of the  
 149 atmospheric correction from the volcano scan method, as well as large noise and spurious  
 150 artifacts that would mask or mimic surface spectral signatures in the 1.0-2.6  $\mu\text{m}$  spectral range.  
 151 Spectra of selected “doublet” units were analyzed from images processed with both methods to  
 152 ensure consistency (Figure 2).  
 153



154  
 155 **Figure 2:** CRISM spectra from selected spots in image FRT0000A202 illustrating “doublet”  
 156 shapes from both types of image techniques: (A) MTRDR, (B) SUBCONV.  
 157

158 We processed images containing a “doublet” feature using a new feature extracting  
 159 algorithm (Saranathan and Parente, 2021) based on Generative Adversarial Networks (GANs).  
 160 GANs are a class of neural network models, called generative models designed to learn and  
 161 mimic the patterns/modalities of a specific dataset. Given their ability to learn the various  
 162 intricacies of a specific dataset from unlabeled samples, they have been successfully used as  
 163 feature extractors to improve the performance of classification (Zhang et al., 2018) and mapping  
 164 algorithms (Saranathan and Parente, 2021) for hyperspectral datasets. The GAN-based mapping  
 165 has proven to be effective in identifying and mapping the boundaries of mineral deposits in  
 166 CRISM images. In this study, the various images were mapped using a base set (of well-known  
 167 mineral shapes known to be present in the CRISM image database) and manually selected  
 168 CRISM spectra representing the most distinct “doublet” type units. The base set of minerals used  
 169 in the mapping are shown in Table 1, these spectral shapes are drawn from the CRISM MICA  
 170 Spectral Library (Viviano et al., 2014). Additionally, we are mapping subtle differences in the  
 171 “doublet” materials and associated minerals in relation to neighboring outcrops using  
 172 hyperspectral factors (i.e., slope, absorption features, etc., see Saranathan and Parente, 2021)  
 173 between 1 – 2.6  $\mu\text{m}$  in the feature extraction procedure rather than just one band, ratio, or slope  
 174 in the spectrum. The manually identified spectral types are listed in Table 1.

175 Output from the GAN mapping is presented in two forms. The IdentMap image displays  
 176 each mineral or material detected in the image in a unique color based on the spectral properties  
 177 over the range 1-2.6  $\mu\text{m}$ . The spectra of these components in the CRISM image are compared to  
 178 a spectral library of minerals and additional materials measured in the lab, as well as to new  
 179 classes identified in the image. In the general case, the GAN mapping technique simply  
 180 compares the GAN space representation of the continuum removed exemplar to that of the  
 181 representation of the continuum removed test pixel (using cosine distance) and assigns a class  
 182 label if appropriate. For the three “doublet” classifications where the variations are subtle, an  
 183 additional fine scale correction is applied to differentiate between the three “doublet”  
 184 classifications. The fine scale correction is only applied to image pixels detected as members of  
 185 one of the “doublet” classifications and focuses on the spectral range of 2.1 – 2.3  $\mu\text{m}$  to  
 186 accurately map these variants. In order to be classified as identifications and to be included in the  
 187 IdentMap image, the CRISM spectra must achieve a cosine similarity  $>0.95$  (Saranathan and  
 188 Parente, 2021) with the shape in the spectral library. However, frequently spectra in CRISM  
 189 images do not perfectly match the spectral library, but still share many similarities with spectra  
 190 of the classes under investigation. This could be due to mixing of multiple materials at a pixel  
 191 level (18 meters), poorly crystalline minerals, or other factors. The GuessMap image includes  
 192 these likely detections that achieve a cosine similarity of 0.85 – 0.95 (Saranathan and Parente,  
 193 2021). The BestGuess image combines the detections made in both the IdentMap and GuessMap  
 194 into a single image.

195 **Table 1:** List of the mineral shapes used for the GAN-based mapping.

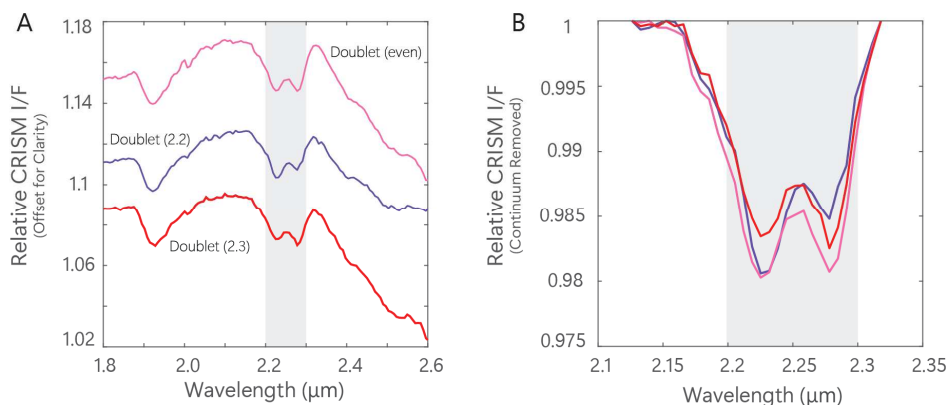
From the MICA List		Manually Identified
Mg-Olivine	Fe-Olivine	Smectite Mix
Mg-Carbonate	Hydrated Silica	Doublet (Stronger 2.2)
Low Ca-Pyroxene	High Ca-Pyroxene	Doublet (Stronger 2.3)
Kaolinite	Illite	Doublet (Even)
Poly Hyd. Sulfate	Mono Hyd. Sulfate	
Alunite	Jarosite	
Gypsum	Prehnite	
Al-Smectite	Fe/Mg-Smectite	
Hyd. Silica	Hydroxylated Fe-Sulfate	
Serpentine	Epidote	

196  
 197 The IdentMap and GuessMap images provide visual maps of the suspected classes of  
 198 minerals and other components. We used these as a guide to check the spectra of individual  
 199 locations, typically 5x5 or 10x10 pixels, but sometimes 3x3 pixel regions for smaller outcrops.  
 200 For these analyses we used ENVI software with the CRISM Analysis Tool (CAT) plugin version  
 201 7.4 available at the NASA's Planetary Data System (PDS) Geosciences Node: <https://pds-geosciences.wustl.edu/missions/mro/crism.htm#Tools>.  
 202

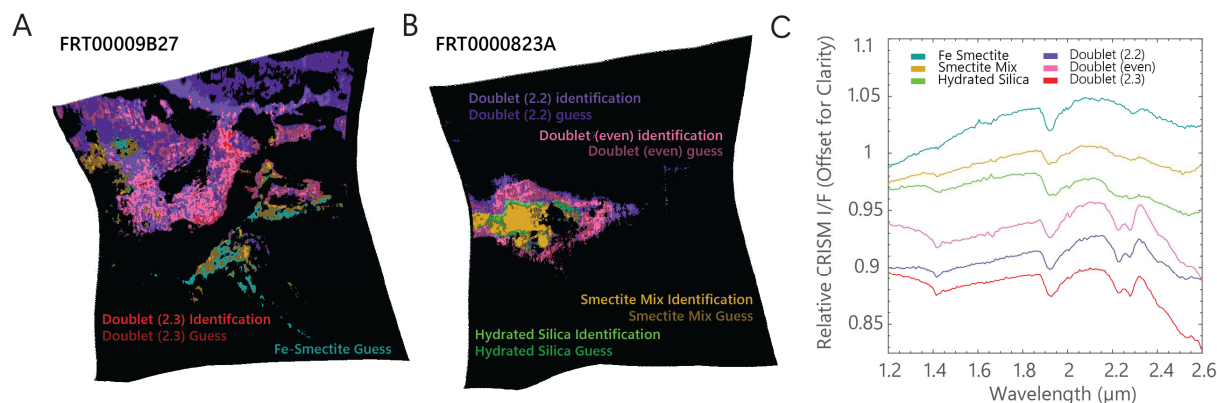
203 Once regions were identified in the image containing a spectral doublet between 2.2 and  
 204 2.3  $\mu\text{m}$ , we classified these into three groups manually: those having a deeper band closer to 2.2  
 205  $\mu\text{m}$ , those having roughly equal band depths, and those having a deeper band closer to 2.3  $\mu\text{m}$   
 206 (Figure 3). CRISM spectra (averaged from several locations to minimize noise) of these three  
 207 new spectral classes were added to the general set of classes identified with the algorithm for all  
 208 CRISM images (Saranathan and Parente, 2021). Figure 4 displays an example of this output,

209 where the BestGuess images include the spectral features of the three newly classified doublet  
210 types, as well as other components. The doublet type spectra are the most common components  
211 in the two example images.

212 We initially analyzed both the MTRDR and SUBCONV images for CRISM images  
213 FRT0000A202, FRT00009B27, and FRT0000823A (Table 2), where the doublet signatures were  
214 strongest to compare the results observed from both techniques. Following the initial  
215 confirmation, we expanded the mapping of the doublet materials and associated minerals along  
216 the southern wall of the northern canyon using SUBCONV and GAN techniques. The GAN  
217 method is optimized for SUBCONV images and cannot be reliably performed for MTRDR  
218 datasets. Additionally, there are no established method for mapping such small variations in the  
219 doublet absorption features using the MTRDR dataset nor other spectral parameters. As such, we  
220 relied on SUBCONV images for our detection and mapping tasks, using the MTRDR images as  
221 a spot check to ensure consistency. We subsequently scanned MTRDR images west of the  
222 doublet materials in both the southern and northern channel that contained light-toned layered  
223 deposits that appeared to have similar morphologies in HiRISE views to the CRISM doublet  
224 materials and prepared SUBCONV and identification maps using the GAN technique; we did  
225 not, however, find evidence of the spectral doublet feature. Additionally, we analyzed MTRDR  
226 image FRT0001751C in the southern channel to characterize the hydrated sulfates located close  
227 to a breach in Geryon Montes and we did not observe the presence of the doublet materials.  
228  
229



230 **Figure 3:** (A) Exemplar spectra of the three classes of “doublet” material added to the mineral  
231 classes for identification. (B) Continuum removed spectra of the three classes of “doublet”  
232 material between 2.1 – 2.3 μm.  
233  
234  
235



236  
237  
238 **Figure 4:** (A) BestGuess view of the “doublet” and other components in CRISM image  
239 FRT00009B27 (B) BestGuess view of the “doublet” and other components in CRISM image  
240 FRT0000823A (C) Example spectra of the different mineral identifications from images  
241 FRT00009B27 and FRT0000823A  
242

### 243 3. Results

#### 244 3.1 Spectral “Doublet” Alteration Product

245 We screened multiple images across Ius Chasma where light-toned outcrops occur, then  
246 selected several CRISM images to investigate in more detail, primarily at the Geryon Montes  
247 site, where these unique spectral doublet features occur at the light-toned units. The CRISM  
248 images evaluated in our detailed study are listed in Table 2.  
249  
250  
251

#### 252 CRISM Images Analyzed

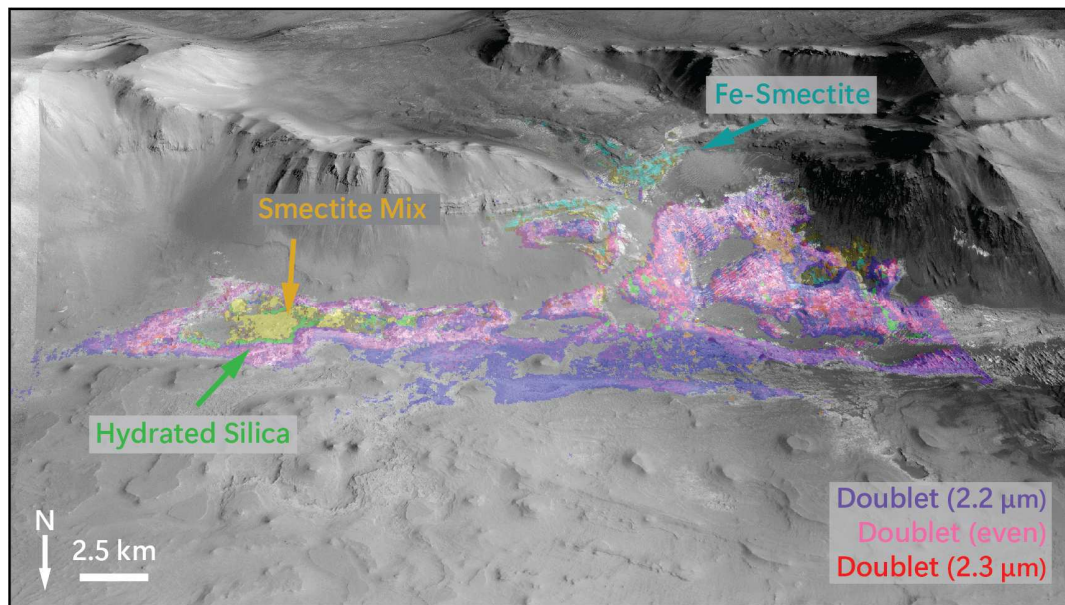
Image	MTRDR	SUBCOM
FRT0000A202	✓	✓
FRT0000A520		✓
FRT00009B27	✓	✓
FRT0000823A	✓	✓
FRT0001712E		✓
FRT00011843		✓
FRT00016626		✓
FRT00009C50		✓
FRT0001135F		✓
FRT0001751C	✓	

253  
254  
255  
256  
257  
258  
259  
260  
261  
262  
263  
264  
265  
266  
267  
268 **Table 2:** List of CRISM images and the calibration techniques used in this study.  
269  
270  
271

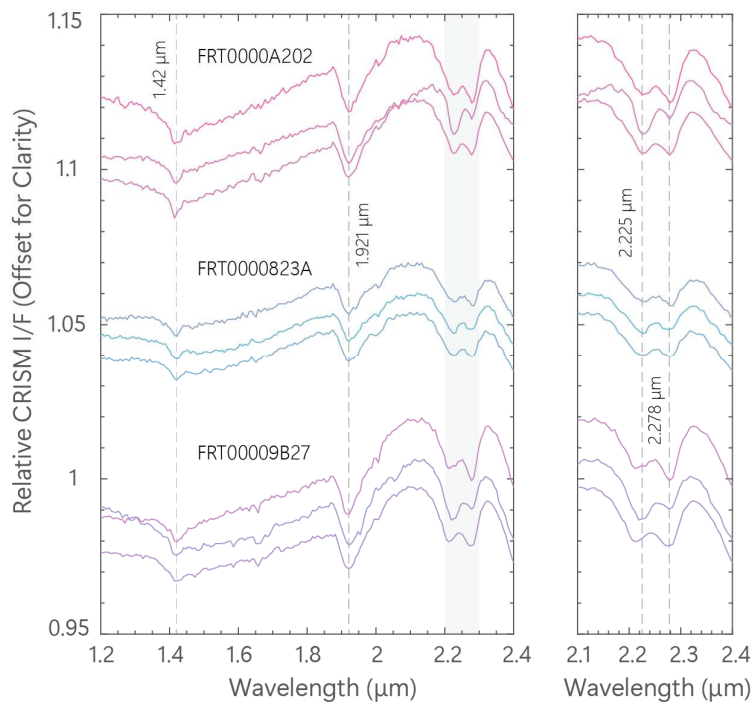
#### 3.1.1 Doublet Characterization:

272 Fe/Mg smectites, opal, and sulfates have been previously identified in the light-toned  
273 deposits within Ius Chasma, in addition to a hydrated mineral phase that was observed with  
274 CRISM data, but not well characterized at Ius Chasma (Roach et al., 2010). This hydrated phase,  
275 referred to here as the “doublet” material, spans across the 35 km light-toned outcrop in central  
276 Ius Chasma, where it is commonly associated with smectites, opal, and mixtures of hydrated  
277 components (Figure 5). The doublet material exhibits absorption features at 1.41 and 1.92  $\mu\text{m}$   
278 due to molecular water, a drop off in reflectance near 2.4  $\mu\text{m}$ , as well as its characteristic spectral  
279 doublet feature that occurs between 2.2–2.3  $\mu\text{m}$ , with the first absorption band occurring  
280 between 2.21 – 2.23  $\mu\text{m}$  and the second absorption band occurring between 2.26 – 2.28  $\mu\text{m}$ .  
281 Most commonly, the absorption features occur at 2.225 and 2.278  $\mu\text{m}$ .

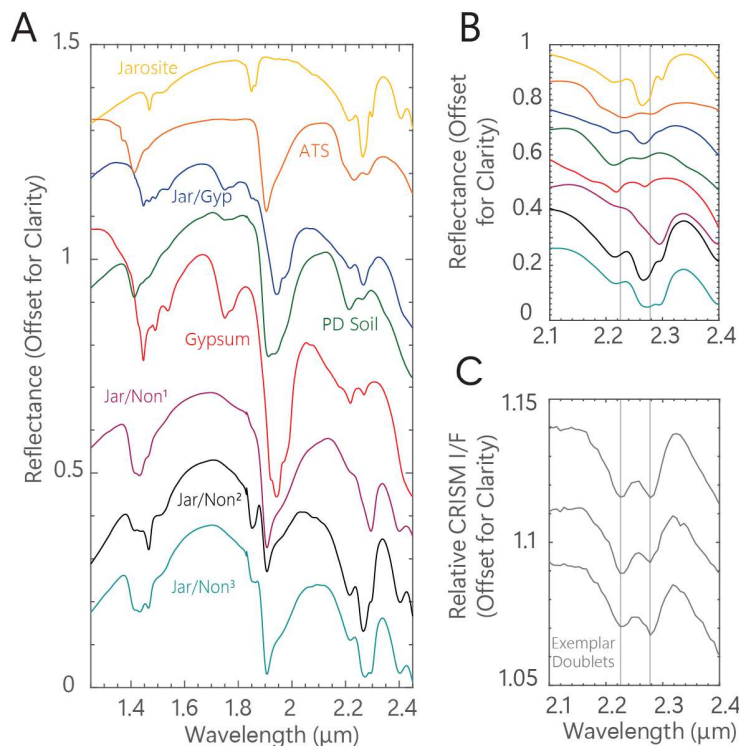
282 We find that the three doublet materials (Figure 3) exhibit high amounts of variation in  
283 the strength of their doublet feature, even when the spectra are averaged over several sites in  
284 which the material has been identified (Figure 6). The band position of these features, however,  
285 remains relatively constant. Previous work could not find a similar or corresponding mineral in  
286 both the RELAB and USGS spectral libraries (Clark et al., 2007) and it was thought that the  
287 closest spectral matches of the doublet material were jarosite, gypsum, or a mixture (Roach et al.,  
288 2010). After re-examining the spectral characteristics of the hydrated doublet materials, we  
289 considered the identity of the doublet material through the comparison of various laboratory  
290 samples that exhibit spectral doublet features between 2.2 – 2.3  $\mu\text{m}$  (Figure 7).  
291



292  
293  
294 **Figure 5:** View of CRISM mineral identification color maps over CTX images on a HRSC  
295 DTM. The three doublet occurrences are mapped in pink (doublet material with equal intensity  
296 2.2 and 2.3  $\mu\text{m}$  bands), purple (doublet material with a stronger 2.2  $\mu\text{m}$  band), and red (doublet  
297 material with a stronger 2.3  $\mu\text{m}$  band), with smectite occurrences in teal and yellow, and other  
298 hydrated silicates mapped in green.



299  
 300 **Figure 6:** The average for each doublet type material across three CRISM image locations in Ius  
 301 Chasma. Notice the variation in band strength between the average doublet types in  
 302 FRT0000A202, FRT0000823A, and FRT00009B27.  
 303



304  
 305 **Figure 7:** (A) Reflectance spectra of minerals and mineral mixtures that exhibit a spectral  
 306 doublet feature between 2.2 – 2.3 μm and were considered in this study: Jarosite (Bishop, 2005),

307 ATS altered for 2 hours (Madejová et al., 2009), a 50/50 wt% jarosite/gypsum mineral mixture  
308 (Jar/Gyp) prepared in the lab (S. L. Perrin et al., 2018), gypsum (Bishop et al., 2014), a 25/75,  
309 75/25, and 50/50 jarosite/nontronite mineral mixture Jar/Non1, Jar/Non2, Jar/Non3 respectively  
310 (Usabal et al., 2019), an orange soil sample from the Painted Desert (PD soil), which includes  
311 ~69 wt% jarosite, ~14 wt% quartz, ~10 wt% gypsum, and ~7 wt% montmorillonite (S. Perrin et  
312 al., 2018). (B) Zoomed in view of the spectral doublet features in laboratory minerals and  
313 mixtures. (C) Exemplar spectra of the three doublet type materials found at Ius Chasma.  
314

### 315 ***3.1.2 Jarosite and Gypsum:***

316  
317 Jarosite ( $\text{KFe}_3^{3+}(\text{OH})_6(\text{SO}_4)_2$ ) exhibits a spectral doublet at 2.21 and 2.26  $\mu\text{m}$  (with the  
318 stronger absorption occurring at 2.26  $\mu\text{m}$ ) due to Fe-OH vibrations, in addition to narrow  
319 absorptions at 1.47 and 1.85  $\mu\text{m}$  due to OH vibrations (Bishop and Murad, 2005; Crowley et al.,  
320 2003). Gypsum ( $\text{CaSO}_4 \cdot 2\text{H}_2\text{O}$ ) also exhibits a spectral doublet at 2.21 and 2.26  $\mu\text{m}$  (with the  
321 stronger absorption occurring at 2.21  $\mu\text{m}$ ), in addition to a distinct triplet absorption between  
322 1.44 and 1.54  $\mu\text{m}$ , as well as absorptions at 1.75 and 1.94  $\mu\text{m}$ , which are due to combinations  
323 and overtones of water vibrations and liberations (Bishop et al., 2014; Cloutis et al., 2006).  
324

325 While both jarosite and gypsum exhibit spectral doublet features between 2.2 – 2.3  $\mu\text{m}$ ,  
326 their spectral doublet band positions, as well as the relative strength and intensities of these  
327 absorption features are not the best match for what is exhibited at Ius Chasma. Additionally, the  
328 doublet materials in Ius Chasma do not exhibit the narrow OH related absorptions at 1.47 and  
329 1.85  $\mu\text{m}$  seen in jarosite, nor do they exhibit the distinct gypsum triplet absorptions between 1.44  
330 and 1.54  $\mu\text{m}$  and the water related absorptions at 1.75 and 1.94  $\mu\text{m}$ .  
331

### 332 ***3.1.3 Jarosite / Gypsum Mixtures:***

333 We considered the possibility that the doublet material may be a mixture of both jarosite  
334 and gypsum, with various jarosite/gypsum ratios creating the three distinct types of doublet  
335 material. A synthetic 50% jarosite/gypsum mineral mixture produces a spectral doublet  
336 characterized by having a weaker ~2.21  $\mu\text{m}$  and a stronger ~2.26  $\mu\text{m}$  absorption feature, in  
337 addition to the gypsum triplet between 1.44 and 1.54  $\mu\text{m}$ , and water related absorptions at 1.75  
338 and 1.94  $\mu\text{m}$  (S. L. Perrin et al., 2018). Spectra of natural jarosite/gypsum mixtures collected  
339 from the Painted Desert soils in Arizona also exhibits a doublet feature with a stronger ~2.21  $\mu\text{m}$   
340 and a weaker ~2.26 absorption band, in addition to spectral features at 1.41, 1.75, and 1.91  $\mu\text{m}$   
341 (S. L. Perrin et al., 2018). While the spectral doublet feature in both the natural and artificial  
342 mixture may be similar to what we are observing at Ius Chasma, the retained spectral character  
343 of jarosite and gypsum make it less likely that the mixture of these minerals are producing the  
344 doublet materials found at Ius Chasma.  
345

### 346 ***3.1.4 Jarosite / Smectite Mixtures***

347  
348 Kaplan et al. (2016) suggested that the doublet material at Ius Chasma may be a  
349 jarosite/smectite mixture. We evaluated a series of synthetic jarosite/nontronite mixtures (Usabal  
350 et al., 2019) containing 25/75, 50/50, and 75/25 wt% jarosite/nontronite, respectively.  
351

352 All three laboratory mixtures have spectral features between 1.41 – 1.47  $\mu\text{m}$ , in addition  
353 to a feature at 1.85  $\mu\text{m}$  in the 75/25 mixture due to OH overtones and combination bands in

353 jarosite, and a water related feature at 1.91  $\mu\text{m}$ . The 50/50 and 25/75 jarosite/nontronite mixtures  
354 produce a spectral doublet feature at  $\sim 2.21$  and  $\sim 2.27$   $\mu\text{m}$ , in addition to a weak 2.29  $\mu\text{m}$  feature.  
355 The 75/25 jarosite/nontronite mixture does not produce a spectral doublet feature, however it  
356 does contain a strong 2.29  $\mu\text{m}$  feature due to OH combination bands in nontronite (Bishop et al.,  
357 2020). While the spectral doublet features in the jarosite/nontronite mixtures may be spectrally  
358 similar to what is observed at Ius Chasma, the absence of jarosite (1.47 and 1.85 $\mu\text{m}$ ) and  
359 nontronite (2.29  $\mu\text{m}$ ) related features in the doublet materials makes it unlikely that the doublet  
360 materials are simply physical mixtures of the minerals jarosite and nontronite.

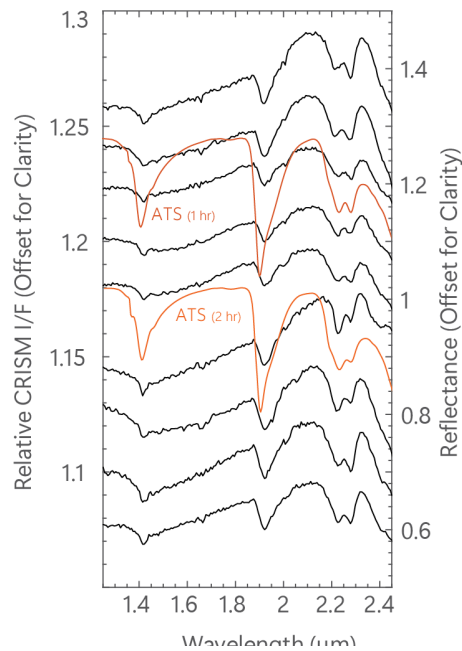
361

#### 362 ***3.1.4 Acid Altered Clays:***

363

364 Given the association between smectites and the doublet material in Ius Chasma, we  
365 considered the possibility that the doublet material may be an alteration product of the smectites  
366 found across the region. We analyzed spectra of an acid treated ferruginous smectite, Swa-1,  
367 measured by Madejová et al., (2009). Several phyllosilicate samples were treated with HCl to  
368 determine the influence of acid alteration on their spectral properties (Madejová et al., 1990,  
369 2007, 2009). These acid treated smectite (ATS) samples have a spectral doublet feature at  $\sim 2.23$   
370 and  $\sim 2.28$   $\mu\text{m}$ , in addition to absorption features at 1.41 and 1.91  $\mu\text{m}$  due to the presence of  
371 molecular water in the sample, and a drop off in reflectance near 2.4  $\mu\text{m}$  (Figure 8). The spectral  
372 similarities of not only the spectral doublet feature, but also other absorption features, found in  
373 both the ATS and doublet materials at Ius Chasma, suggests that the doublet material may be an  
374 acid altered smectite mineral. Variations in the relative strengths of the doublet bands were also  
375 observed due to changes in the length of acid treatment (Madejová et al., 1990, 2007, 2009),  
376 where a stronger band was observed near 2.23  $\mu\text{m}$  for a longer exposure to acidic conditions. We  
377 favor formation of the doublet materials at Ius Chasma through acid alteration of the smectites,  
378 with the doublet variation attributed to differences in the solution chemistry, water/rock ratio,  
379 substrate, or duration of the alteration process.

380



381  
 382 **Figure 8:** Spectra of several Ius Chasma doublet sites compared to two acid treated smectite  
 383 (ATS) samples altered for one and two hours (see Madejová et al., 2009) in orange. The ATS  
 384 samples display the most spectral similarities to the doublet materials, as they display similar  
 385 water band positions at  $\sim 1.41$  and  $\sim 1.91$   $\mu\text{m}$ , in addition to strikingly similar doublet features at  
 386  $\sim 2.23$  and  $\sim 2.28$   $\mu\text{m}$ , as well as a drop off in reflectance at  $\sim 2.4$   $\mu\text{m}$ .  
 387

### 388 3.2 Properties of Materials and Geomorphology of the Geryon Montes Region of Ius 389 Chasma

390 Ius Chasma is connected to Noctis Labyrinthus in the west and to Melas Chasma in the  
 391 east, stretching nearly 850 kilometers in length and 120 kilometers in width. Within Ius Chasma  
 392 are tributary canyons, with the longest most prominent tributary canyon containing the light-  
 393 toned deposits. The surface of the light-toned deposits at Ius Chasma are characterized by their  
 394 polygonal fractures which could have formed through the desiccation of hydrated materials or  
 395 thermal contraction. These light-toned deposits are described in depth by (Roach et al., 2010).

396 The mountains that make up Geryon Montes separate Ius Chasma into southern and  
 397 northern canyons, reaching heights upwards of 5 kilometers and local widths of up to 26  
 398 kilometers (Dębnia et al., 2017). The northern canyon of Ius Chasma contains smectites and  
 399 other hydrated silicates, whereas the southern canyon contains both MHS and PHS (Figure 9)  
 400 and shows no evidence of containing doublet like materials. These sulfates likely evaporated  
 401 from a concentrated parent brine that pooled within the southern canyon (Roach et al., 2010),  
 402 with the brine initially precipitating out PHS followed by MHS near the end stages of  
 403 evaporation (Spencer, 2000). The sulfates observed at Ius Chasma on the south side of Geryon  
 404 Montes are similar to the MHS and PHS observed in other chasmata and likely needed long-term  
 405 warm waters (Al-Samir et al., 2017). The smectite-bearing units and hydrated silica found in the  
 406 northern canyon are typical of these materials observed elsewhere on Mars in the ancient  
 407 Noachian rocks (e.g Mustard et al., 2008). The most prominent aqueous outcrop after the doublet

408 units is the smectite mixture mapped in gold that contains some spectral features of Fe/Mg-  
409 smectite with a weaker band near 2.3  $\mu\text{m}$ . Occasional occurrences of Fe-rich smectite with a  
410 band near 2.29  $\mu\text{m}$  are mapped in teal and are generally observed in outcrops not bordering the  
411 smectite mixture materials. The hydrated silica unit (green) is more common than the Fe-rich  
412 smectite and typically does border the smectite mixture unit. Example spectra of these units are  
413 shown in Figure 4.

414 Mineral identification maps are presented in Figs. 5, 10a, and 11. Smectite mixture  
415 occurrences are mapped in yellow, iron smectites are mapped in teal, hydrated silica is mapped  
416 in green, with the doublet occurrences mapped in pink (doublet characterized by having equal  
417 intensity 2.2 and 2.3  $\mu\text{m}$  bands), purple (doublet characterized by having a stronger 2.2  $\mu\text{m}$   
418 band), and red (doublet characterized by having a stronger 2.3  $\mu\text{m}$  band). The morphologies of  
419 the doublet materials located in the northern canyon are shown in Figure 10a. The pink and  
420 purple units mapped with CRISM correspond to fractured and brecciated light-toned materials.  
421 Smooth ridges can be present with a general N-S orientation, consistent with erosion by  
422 downslope and upslope winds along the steep walls of the canyon. Brightness variations are  
423 common but do not correspond to specific layers or elevations. Some irregular patches within the  
424 pink and purple doublet units are much brighter than the adjacent materials indicating  
425 compositional and/or physical heterogeneities in these deposits. The most prominent difference  
426 in morphology between the pink and purple colors appears to be due to the presence of darker  
427 loose sediments on the surface of the purple unit (Fig. 10c) that is not seen on the pink unit (Fig.  
428 10b). Note that these “darker” loose sediments are darker than the pink unit, but still brighter  
429 than the surrounding materials. Coverage of the red doublet (stronger 2.28  $\mu\text{m}$  band) is limited in  
430 HiRISE image ESP\_048136\_1725 and thus it is difficult to determine differences in morphology  
431 of the red unit compared to the pink and purple units.

432 One possible explanation for the relationship between the pink and purple units is that the  
433 darker loose sediments contain a band near 2.2  $\mu\text{m}$  but not near 2.3  $\mu\text{m}$  and that they partially  
434 cover the pink unit, resulting in a stronger intensity of the 2.23  $\mu\text{m}$  band of the doublet when  
435 viewed by CRISM at 18 m spatial resolution. This could be possible if the loose sediment  
436 contains opal. Spectral mixing of the broad hydrated silica-type band near 2.1  $\mu\text{m}$  with the  
437 narrower 2.23  $\mu\text{m}$  band observed for the doublet outcrops could result in a stronger band at 2.23  
438  $\mu\text{m}$  compared to 2.28  $\mu\text{m}$  with only a minor shift in band position near 2.23  $\mu\text{m}$ . Another  
439 interpretation is that the darker loose sediments are sourced from a more strongly altered material  
440 where the 2.23  $\mu\text{m}$  band is stronger compared to the 2.28  $\mu\text{m}$  band. Potentially, the more altered  
441 unit is less cohesive and eroded faster through wind erosion, becoming a mobile sediment unit.  
442 In this scenario the pink materials would have experienced more acidic alteration than the red  
443 materials and the purple unit would have experienced the most acidic alteration but is no longer a  
444 coherent material, but rather mobile and partially covering the pink unit. This would explain  
445 variations in the intensities of the doublet bands.

446 In the case of the green (hydrated silica) and gold (Fe/Mg-smectite mixture) units, both  
447 appear to have a surficial veneer of darker materials making them lower in brightness relative to  
448 the pink and purple units. Meter-scale layering is present throughout much of the gold unit, as  
449 are aeolian ripples. The smooth N-S ridges commonly seen in the pink and purple units are not  
450 observed in the gold unit. Instead, rough blocky ridges and knobs shedding large boulders are  
451 seen only in the gold unit. The difference in morphology between the green and gold units is not  
452 well constrained from the HiRISE images. Thus, there appear to be primarily two distinct units

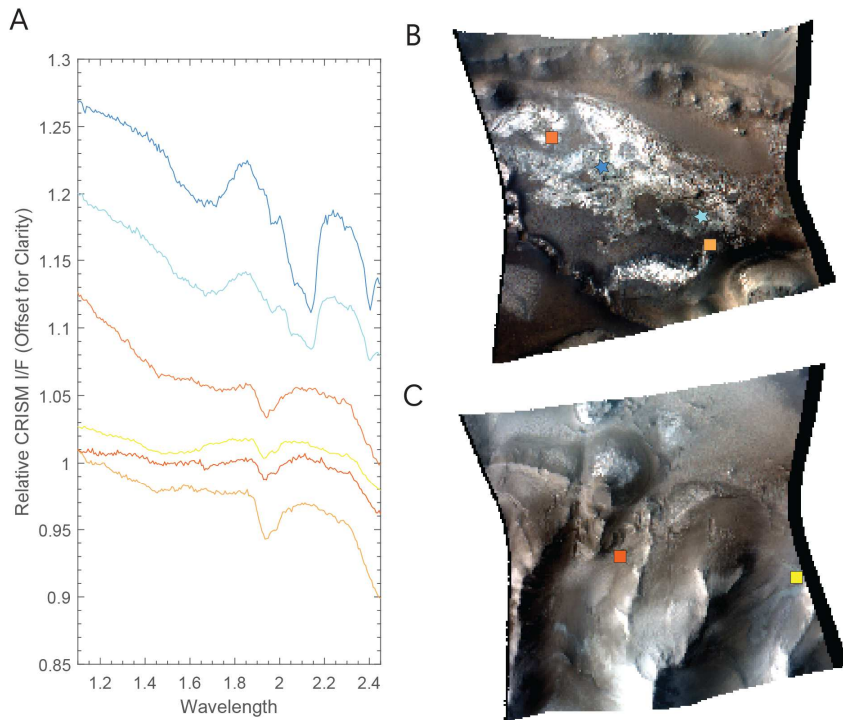
453 based upon morphology, with the pink and purple colors representing one unit (with the thicker  
454 dark surficial mantle occurring on the purple colored regions) and the gold and green colored  
455 materials representing a different unit.

456 The stratigraphy for the different colors does not correlate to elevation as shown by the  
457 DTM perspective view and topographic profile shown in Figure 11. All the units are draped  
458 along the lower wall rock slopes of northern Geryon Montes between elevations ~-3600 m to -  
459 4100 m. Both the green and purple colored regions correspond to shallower slopes relative to the  
460 pink and gold colored regions. Because loose debris is more favorable to collect on shallower  
461 surfaces, the purple and green areas are more likely to have more dark debris on their surfaces  
462 that in turn would affect the CRISM spectra relative to the pink and gold regions.

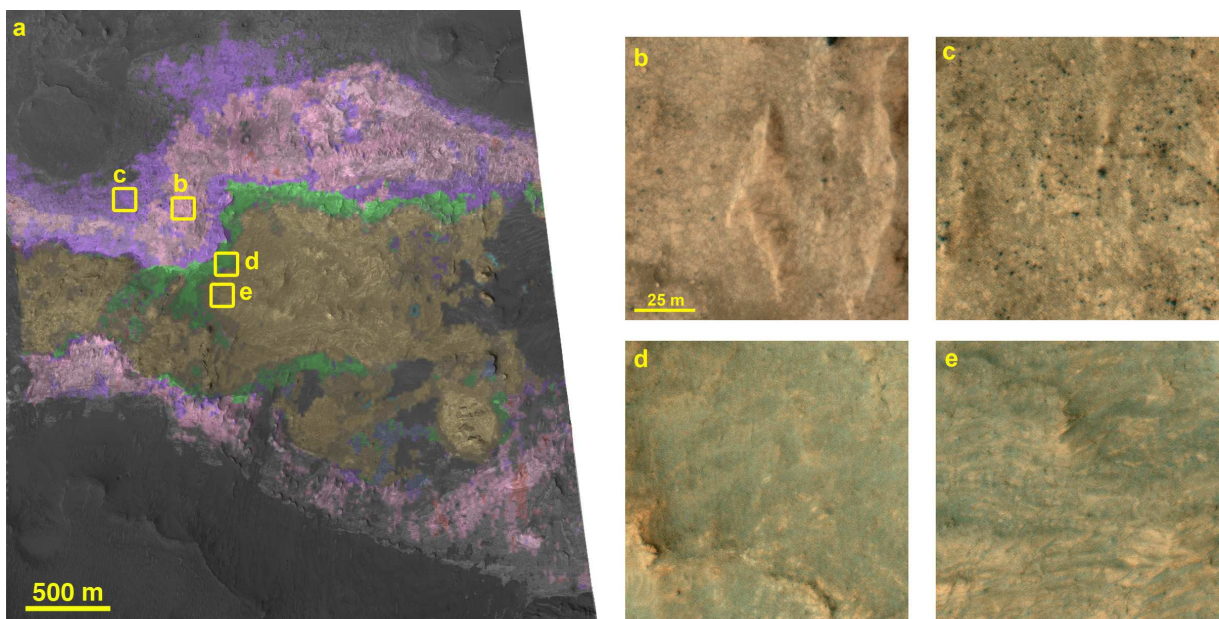
463 Topography derived from MOLA data has also been useful for understanding why the  
464 doublet materials could have formed here. The section of Geryon Montes mountains that  
465 collocates with the doublet material in Ius Chasma has a significantly lower ridge height than  
466 ridge localities to both the east and west of the observed doublet unit (Figure 12). It is likely that  
467 pooling water forming the parent brine in the southern sulfate-rich canyon overflowed at the  
468 breach in Geryon Montes where the topography shows the lowest height over the ridge formation  
469 into the northern canyon where the doublet materials are observed. The morphology and  
470 topology observed along the upper deposit exhibits rounded edges, heterogeneity, and  
471 topography variations (Figure 13) that are consistent with fluid flow in this region and therefore  
472 supportive of an inflow of brine from the southern canyon. The jumbled, blocky morphology  
473 observed here at Ius Chasma is similar to the blocky deposits identified along the wall rock and  
474 floor to the east in Melas Chasma. The Melas deposits have been interpreted as evidence for soft  
475 sediment deformation by slumping and/or sliding of sulfates and clay mixtures down the wall  
476 rock slopes (Metz et al., 2010; Weitz et al., 2015), consistent with our proposed flow origin for  
477 the Ius Chasma deposit.

478 As the brine overflowed from the southern to northern canyons at this gap in Geryon  
479 Montes, the brine likely flowed down the wall rock following the slope of the canyon and  
480 penetrated into the rock. If substantial flows had occurred, the largest alteration outcrops would  
481 have occurred along the floor of the northern canyon. Because we observe the greatest  
482 abundance of alteration phases exposed along the lower slopes of the wall rock, the brine flows  
483 appear to have been concentrated in these regions, rather than on the floor of the north channel.  
484 We propose that these sulfate-rich brines altered the phyllosilicates in or on the wall rock to form  
485 the doublet materials. The transect in Figure 11 shows that the doublet materials are present  
486 above and below the phyllosilicates and hydrated silica. This may indicate that these ancient  
487 smectites were altered by the brine both along the exposed surfaces, as well as along the borders  
488 of the smectite units if brine was able to seep through the regolith and more aggressively alter  
489 these smectite outcrops along the edges. Thus, thinner regions of smectite along the edges of the  
490 outcrop could be nearly completely altered, while the thicker smectite-bearing regions near the  
491 center of the outcrop are still partially intact in the wall rock. These thicker regions likely  
492 contained a veneer of brine-altered material on their surface initially that was then scoured off  
493 over time. In contrast, the regions where the doublet materials are observed today could have  
494 initially been thinner smectite deposits that became doublet units during alteration and are still  
495 observed today, although the original surface of the doublet material was likely scoured off over  
496 time. Alternatively, given that the doublet unit is observed both to the west at Noctis Labyrinthus  
497 and to the east in Melas Chasma, the unit may have originally been deposited as a volcanic ash

498 unit (containing smectites) across the region and then subsequently altered as described above by  
499 the brine overflowed at this gap.  
500

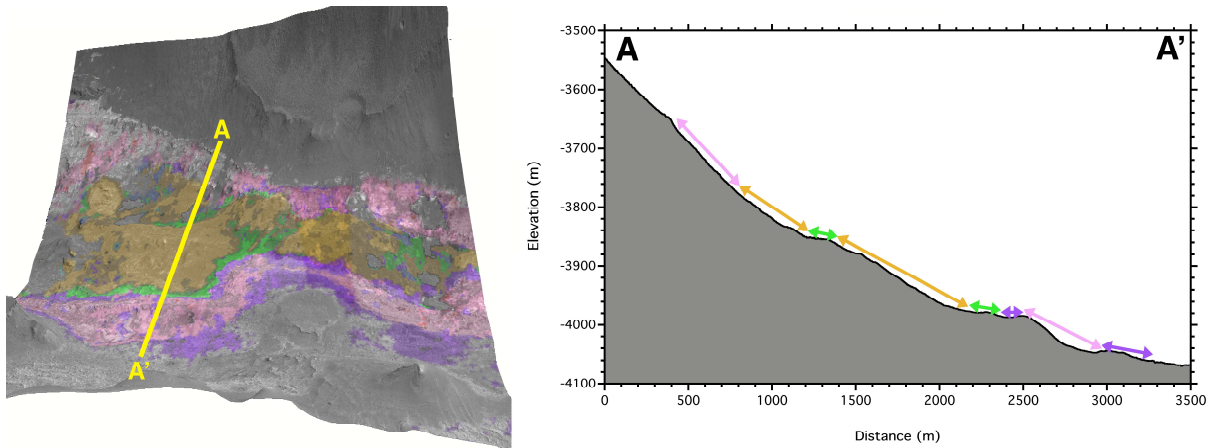


501  
502 Figure 9: (A) Spectra of the monohydrated sulfates (MHS) and polyhydrated sulfates (PHS) in  
503 the southern canyon (B) Views of the southern canyon of Ius Chasma in CRISM images  
504 FRT00016626 and (C) FRT00011843. Locations marked with squares correspond to the PHS  
505 and locations marked with stars correspond to the MHS shown in (A).

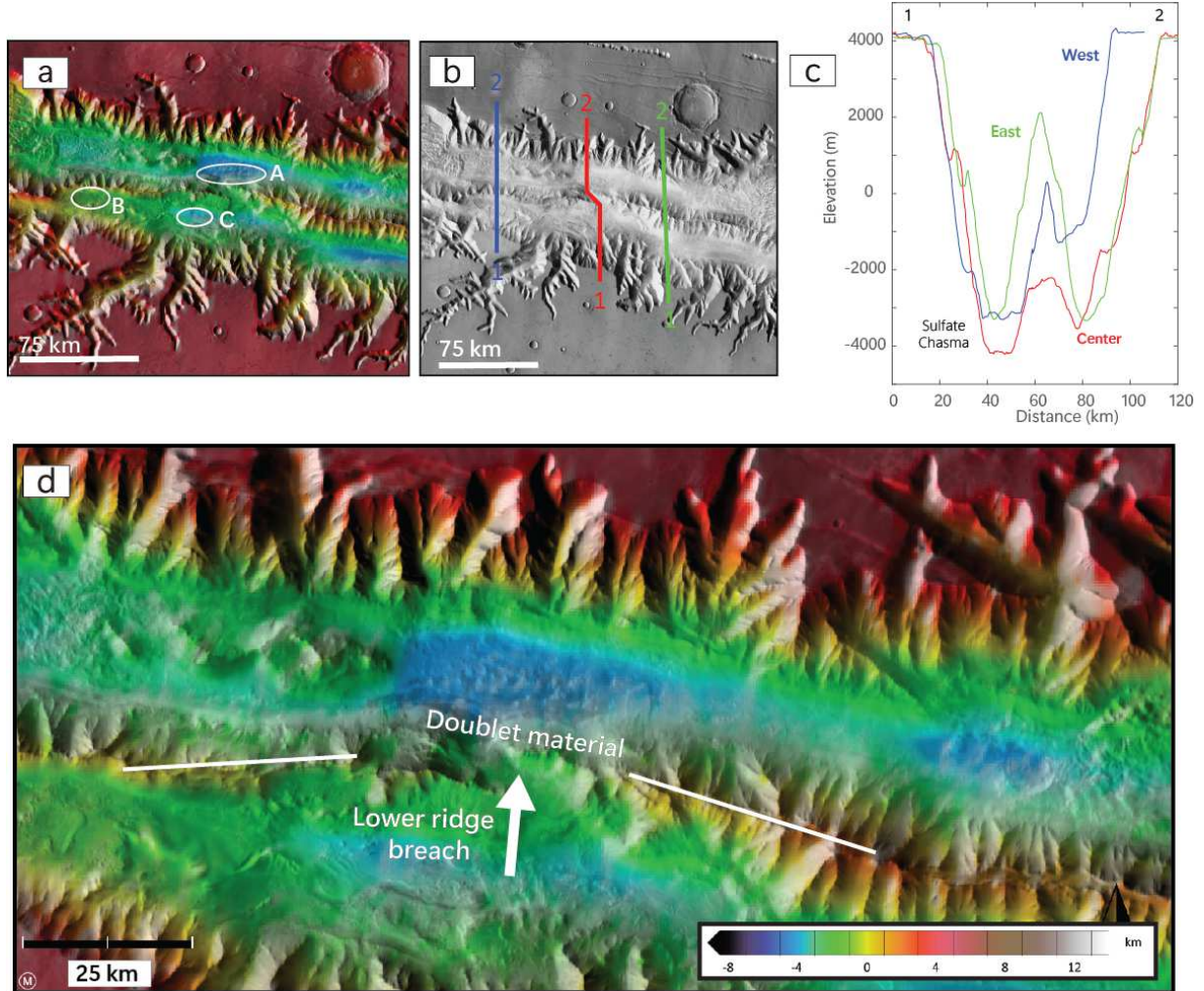


506

507 Figure 10: (a) HiRISE RED image ESP\_048136\_1725 with spectral units from CRISM image  
 508 FRT0000823A mapped using the same color scheme in Figure 5. The three doublet occurrences  
 509 are mapped in pink (doublet material with equal intensity 2.2 and 2.3  $\mu\text{m}$  bands), purple (doublet  
 510 material with a stronger 2.2  $\mu\text{m}$  band), and red (doublet material with a stronger 2.3  $\mu\text{m}$  band),  
 511 with smectite occurrences in yellow and other hydrated silicates mapped in green. Yellow  
 512 squares identify blowups in b-e. (b-e) Blowups taken from HiRISE ESP\_048136\_1725 RGB  
 513 image showing the morphologies corresponding to the different colors. Scale bar in (b) is the  
 514 same for (c-e).



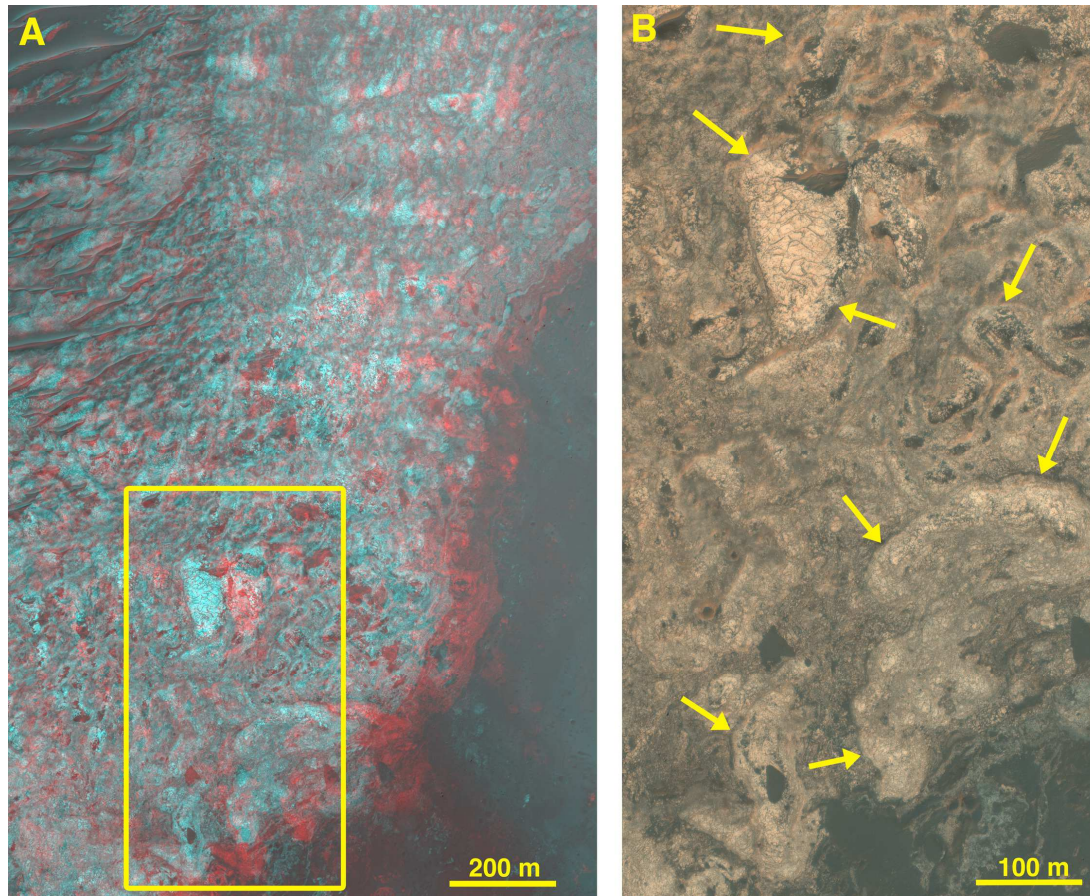
515  
 516 Figure 11: (left) HiRISE DTM perspective view at 3x V.E. with the same color scheme for the  
 517 CRISM mineral map in Figures 5 and 10 overlain. The three doublet occurrences are mapped in  
 518 pink (doublet material with equal intensity 2.2 and 2.3  $\mu\text{m}$  bands), purple (doublet material with  
 519 a stronger 2.2  $\mu\text{m}$  band), and red (doublet material with a stronger 2.3  $\mu\text{m}$  band), with smectite  
 520 occurrences in yellow and other hydrated silicates mapped in green. The location where the  
 521 topographic profile was taken is shown by the yellow line. (right) Topographic profile showing  
 522 the locations of each spectral color by the arrows with the same colors. Note how the units drape  
 523 along the lower wall rock slopes and do not correspond to a particular elevation.



524

525 Figure 12: (A) Views of Ius Chasma indicating the locations of doublet materials (a) and  
 526 two sites containing sulfates (b,c). (B) THEMIS daytime image with three profile line marked. (C)  
 527 Profile from N to S across Geryon Montes and the sulfate-bearing side of the chasma for the  
 528 western, central, and eastern profiles. Note the low elevation of the Geryon Montes mountains  
 529 associated with the center profile (red) and the low elevation of the northern canyon floor where  
 530 the doublet materials were found. (D) MOLA topography with lower depths shown in blue. The  
 531 white lines show the top of the Geryon Montes mountains, and the white arrow identifies the  
 532 lowest elevation along the mountains where there appears to be a breach from the south to the  
 533 northern canyon.

534



535

536 Figure 13: Example of the jumbled, deformed morphology of the Ius deposit at the location of  
 537 the wall rock breach in Geryon Montes. (A) HiRISE anaglyph showing the uneven topography  
 538 across the deposit, with a higher standing heterogeneous darker matrix above rounded, brighter  
 539 materials. HiRISE stereo images ESP\_060136\_1725 and PSP\_007074\_1725 were used to  
 540 produce this anaglyph. Yellow rectangle identifies the blowup shown in (B). (B) Rounded edges  
 541 identified by yellow arrows do not always follow the slope along the wall rock (from lower right  
 542 to upper left) and are variable in topography, consistent with flow of the doublet unit downhill  
 543 rather than intact bedrock exposed within the wall rock. Portion of HiRISE enhanced RGB  
 544 image ESP\_060136\_1725.

545

#### 546 4. Potential geochemical formation processes

547

##### 548 4.1 Overflow from south canyon

549

550 Phyllosilicates are observed together with sulfates throughout much of the region from  
 551 Noctis Labyrinthus to Ius Chasma and Melas Chasma and may have resulted from aqueous  
 552 alteration of pyroclastic ash deposits (Weitz et al., 2010). Fe/Mg-smectites are observed  
 553 throughout the southern highlands of Mars and are thought to have formed through aqueous  
 554 alteration of basalt during the Noachian (e.g. Murchie et al., 2009a; Bishop et al., 2018). Spectral  
 555 doublet units occur in a few localities on Mars including Noctis Labyrinthus (Weitz et al., 2011)  
 556 and Mawrth Vallis (Bishop et al., 2020), with the largest outcrop observed at Ius Chasma on the  
 557 north side of Geryon Montes. Smectites alter in acidic solutions to form a spectral doublet  
 558 feature (Madejová et al, 2009), which is likely what occurred at Geryon Montes. We posit that

559 this doublet material formed by brine overflowing from the MHS/PHS pool on the south of  
 560 Geryon Montes to form a brine-sludge on the south wall of the northern canyon along Geryon  
 561 Montes as the brine interacted with fine-grained particles, including phyllosilicates. Brine  
 562 viscosity increases with sulfate and chloride content as well as with the presence of insoluble  
 563 fines and lower temperatures (e.g., Chevrier et al., 2009; Sánchez-Juny et al., 2019). If the brine  
 564 had been a liquid-like low viscosity consistency, it would have flowed to the floor of the canyon  
 565 and altered the materials there. Instead, we observed the strongest outcrops of the doublet  
 566 material along the south wall slopes of this northern canyon which suggests a higher viscosity for  
 567 the brine-sludge. Another possibility is that neutral or dilute waters along the floor of the  
 568 northern channel served to dilute the brine concentration at lower elevations. This scenario is less  
 569 likely though because if a standing brine was present in the north channel, we would expect to  
 570 see evidence of alteration minerals along the floor and these are not observed. Other regions of  
 571 the wall containing hydrated silica may have formed from brine alteration of basaltic ash where  
 572 smectites were not present in the ancient canyon walls. A similar process could have occurred at  
 573 neighboring canyons where doublets are also observed. Because the doublet materials at Ius  
 574 Chasma have the strongest spectral features relative to other locations, they appear to be the most  
 575 concentrated occurrence of this unique alteration phase.  
 576



577  
 578  
 579 Figure 14: Proposed formation sequence of the doublet materials at Ius Chasma: (1) Ancient  
 580 smectite outcrops, either exposed within the wall rock as bedrock or super imposed on it as  
 581 volcanic ash, along the southern wall of the northern Geryon Montes canyon in Ius Chasma. (2)  
 582 Sulfate brines pooled in the southern canyon where sulfates formed, then overflowed into the  
 583 northern canyon, seeping down the canyon wall, but not extending to the canyon floor. (3)  
 584 Interaction with the brine solution would have altered the smectites to form the doublet material,  
 585 with changes in the solution chemistry, water/rock ratio, or time of alteration creating the  
 586 differences in doublet material.  
 587

#### 588 4.2 Comparison with terrestrial analog sites

589 Terrestrial analog sites featuring phyllosilicate-sulfate assemblages provide insights into  
 590 potential geochemical environments governing formation of this doublet spectral feature. The Ius  
 591 Chasma outcrop at Geryon Montes is consistent with alteration of pre-existing Fe/Mg-smectite  
 592 to form large outcrops of three types of spectral doublet units along with minor occurrences of  
 593 Al-phyllosilicates and hydrated silica. This transition from Fe-rich smectite to sulfate/silica/Al-  
 594 phyllosilicate assemblages can provide evidence about the geochemical history of the region  
 595 including changes in pH, salt levels, and/or water/rock ratio.

596 Evaporite environments supporting salars or shallow salt ponds in the Antofagasta region  
 597 of Chile, north of the Atacama desert include assemblages of gypsum, halite, hydrated silica, and  
 598 phyllosilicates (Flahaut et al., 2017). Many of the gypsum-bearing rocks and sediments from that  
 599 study exhibit spectral doublet features, although they are weaker than those observed at Ius  
 600 Chasma. Similar rocks and sediments have been observed in salt ponds of the Yilgarn Craton of

601 Western Australia, where mixtures of phyllosilicates, opal, gypsum, alunite, and jarosite have  
602 been investigated (Benison and Bowen, 2006; Bowen et al., 2013; Story et al., 2010). Based on  
603 these analog sites, evaporites alone would not be good analogs for the Ius Chasma site, but brines  
604 similar to some of these evaporite sites could have altered the ancient smectites at Ius Chasma to  
605 form the observed doublets.

606 Solfataric alteration of volcanic ash at Kilauea, HI (Bishop et al., 2005) and LaSolfatara,  
607 Italy (Flahaut et al., 2019) has produced mixtures of nontronite, jarosite, gypsum, and opal.  
608 While this scenario is unlikely to explain the doublet unit observed at Ius Chasma, this scenario  
609 may provide a viable explanation for the doublet units observed at other regions on Mars.

610 The extensive doublet units observed at Ius Chasma are attributed to a more regional  
611 process and could be due to alteration of the ancient Fe/Mg-smectite present in Noachian basalt  
612 or volcanic ash in a muddy sludge-type setting as the brine interacts with the phyllosilicates and  
613 associated fine-grained materials of this region. The presence of different types of doublet units  
614 here is consistent with changes over time in the pH, salt levels, or water/rock ratio, or simply  
615 with the degree of alteration of the smectite in the acidic sludge. Madejová et al. (2009)  
616 documented changes in the intensity of the spectral doublet feature in smectites with progressive  
617 acidic alteration in the laboratory. This is most consistent with the changes in relative abundance  
618 of the doublet bands in our study.

619

#### 620 **4.3 Summary**

621

622 Previous work (Kaplan et al., 2016; Roach et al., 2010) investigated the enigmatic  
623 materials found in the light-toned deposits at Ius Chasma, although the identity of the doublet  
624 materials remained unresolved at that time. Here we re-examined the potential composition of  
625 the doublet material with improved image calibrations and detailed mapping of the doublet  
626 occurrences. These significantly improved spectral images allowed for documentation of  
627 variations among the doublet-type units, and three types of doublet units were identified and  
628 mapped along the wall of the northern canyon of Ius Chasma near the breach in the Geryon  
629 Montes. The spectra of the Ius Chasma doublets exhibit water bands near 1.4 and 1.9  $\mu\text{m}$ , similar  
630 to smectite clays, as well as a pair of narrow bands near 2.23 and 2.27  $\mu\text{m}$  that vary in relative  
631 intensity. The relative intensities of these doublet bands were used to define three units: where  
632 both bands have similar band strengths, where the  $\sim 2.23 \mu\text{m}$  band is stronger, and where the  
633  $\sim 2.27 \mu\text{m}$  band is stronger.

634

635 Three possible compositions of the doublet material at Ius Chasma were investigated:

636

1) Jarosite / gypsum mixture

637

2) Jarosite / smectite mixture

638

3) Acid altered smectite

639

640 None of these potential compositions and formation mechanisms provides a perfect fit for the  
641 spectral properties of the doublet materials in our study. However, of these possibilities, we favor  
642 the acid alteration scenario whereby the doublet material at Ius Chasma forms where acidic  
643 brines altered pre-existing smectites in or on the wall rock. Variations in the doublet material  
644 may be attributed to compositional changes in the underlying substrate, changes to the solution  
645 chemistry in the pooling waters over time, or simply duration of the brine and hence extent of  
646 alteration.

647 Correlation of the mineral maps from CRISM with the higher spatial resolution of HiRISE  
648 enabled comparison of the morphologies of the different alteration units at meter scale. These  
649 results indicated similarities in the smectite-mixture unit and the hydrated silica unit as well as  
650 similarities among the doublet units. These observations are consistent with a common origin for  
651 the different doublet units. Mapping transects of these components along the wall rock using  
652 CRISM results overlain on a HiRISE DTM shows shallower slopes where the hydrated silica and  
653 purple-colored doublet units are present. This may indicate collection of more dust and mobile  
654 components at these locations.

655 Correlation of the mineral maps from CRISM with the HRSC stereo views provides geologic  
656 context across several CRISM images and documents formation of the doublet units surrounding  
657 the smectite in some cases, likely where a thicker smectite unit existed prior to brine deposition.  
658 Other regions of the aqueous outcrops are dominated by the doublet materials, leaving few  
659 remnants of the smectite visible at the surface. This could have occurred where the original  
660 smectite units were thinner and more readily altered by the acidic brine and/or where thicker acid  
661 altered smectite units were produced. The stratigraphy and locations of the alteration materials in  
662 the CRISM over HRSC view (Figure 5) also shows that the largest smectite outcrop occurs  
663 further from the breach in the Geryon Montes and that most of the altered materials directly  
664 below the breach are completely altered to the doublet units described in our study. Further, the  
665 purple-colored doublet unit that contains a stronger 2.23  $\mu\text{m}$  band and is consistent with  
666 increased acid alteration, occurs downslope from the less altered doublet outcrops. This supports  
667 our brine alteration model in that the lower elevation, shallower sloped horizon below the breach  
668 at Geryon Montes exhibits the strongest alteration.

## 669 **5. Acknowledgements**

670  
671 We greatly appreciate the efforts of the CRISM, HiRISE, and HRSC teams for collecting  
672 and archiving the images used in this study. We are grateful to support from the NASA  
673 Astrobiology Institute (grant #NNX15BB01) to JLB, NASA's Mars Data Analysis Program  
674 (grant #NNX19K1230) to JLB, CMW, and KW, and NASA's Planetary Data Archiving,  
675 Restoration, and Tools Program (grant #NNX16AG48G) to MP, YI, and AMS for this work. We  
676 are also thankful for suggestions from L. Roach, S. Murchie, and E. Rampe that improved this  
677 paper.

678

679

## 680 **6. References**

681

682 Al-Samir, M., Nabhan, S., Fritz, J., Winkler, A., Bishop, J.L., Gross, C., Jaumann, R., 2017. The  
683 paleolacustrine evolution of Juventae Chasma and Maja Valles and its implications for  
684 the formation of interior layered deposits on Mars. *Icarus* 292, 125–143.  
685 <https://doi.org/10.1016/j.icarus.2016.12.023>

686 Benison, K., Bowen, B., 2006. Acid saline lake systems give clues about past environments and  
687 the search for life on Mars. *Icarus* 183, 225–229.  
688 <https://doi.org/10.1016/j.icarus.2006.02.018>

689 Bibring, J.-P., Langevin, Y., Mustard, J.F., Poulet, F., Arvidson, Raymond, Gendrin, A., Gondet,  
690 B., Mangold, N., Pinet, P., Forget, F., Berthé, M., Bibring, J.-P., Gendrin, A., Gomez, C.,  
691 Gondet, B., Jouglet, D., Poulet, F., Soufflot, A., Vincendon, M., Combes, M., Drossart,

692 P., Encrenaz, T., Fouchet, T., Merchiorri, R., Belluci, G., Altieri, F., Formisano, V.,  
693 Capaccioni, F., Cerroni, P., Coradini, A., Fonti, S., Korablev, O., Kottsov, V., Ignatiev,  
694 N., Moroz, V., Titov, D., Zasova, L., Loiseau, D., Mangold, N., Pinet, Patrick, Douté, S.,  
695 Schmitt, B., Sotin, C., Hauber, E., Hoffmann, H., Jaumann, R., Keller, U., Arvidson, Ray,  
696 Mustard, J.F., Duxbury, T., Forget, François, Neukum, G., 2006. Global Mineralogical  
697 and Aqueous Mars History Derived from OMEGA/Mars Express Data. *Science* 312,  
698 400–404. <https://doi.org/10.1126/science.1122659>

699 Bishop, J.L., Flahaut, J., Perrin, S.L., 2019. Characterizing environments containing complex  
700 phyllosilicate-sulfate assemblages as analogs for Mars. Presented at the EPSC-DPS Joint  
701 Meeting, Geneva, Switzerland.

702 Bishop, J.L., Gross, C., Danielsen, J., Parente, M., Murchie, S.L., Horgan, B., Wray, J.J.,  
703 Viviano, C., Seelos, F.P., 2020. Multiple mineral horizons in layered outcrops at Mawrth  
704 Vallis, Mars, signify changing geochemical environments on early Mars. *Icarus* 341,  
705 113634. <https://doi.org/10.1016/j.icarus.2020.113634>

706 Bishop, J.L., Lane, M.D., Dyar, M.D., King, S.J., Brown, A.J., Swayze, G.A., 2014. Spectral  
707 properties of Ca-sulfates: Gypsum, bassanite, and anhydrite. *American Mineralogist* 99,  
708 2105–2115. <https://doi.org/10.2138/am-2014-4756>

709 Bishop, J.L., Murad, E., 2005. The visible and infrared spectral properties of jarosite and alunite.  
710 *American Mineralogist* 90, 1100–1107. <https://doi.org/10.2138/am.2005.1700>

711 Bishop, J.L., Parente, M., Weitz, C.M., Noe Dobrea, E.Z., Roach, L.H., Murchie, S.L., McGuire,  
712 P.C., McKeown, N.K., Rossi, C.M., Brown, A.J., Calvin, W.M., Milliken, R., Mustard,  
713 J.F., 2009. Mineralogy of Juventae Chasma: Sulfates in the light-toned mounds, mafic  
714 minerals in the bedrock, and hydrated silica and hydroxylated ferric sulfate on the  
715 plateau. *J. Geophys. Res.* 114, E00D09. <https://doi.org/10.1029/2009JE003352>

716 Bishop, J.L., Schiffman, P., Lane, M.D., Dyar, M.D., Southard, R.J., 2005. Solfataric alteration  
717 in Hawaii as a mechanism for formation of the sulfates observed on Mars by OMEGA  
718 and the MER instruments. Presented at the Lunar Planet. Sci. XXXVI, Houston, TX.

719 Bishop, J.L., Schiffman, P., Lane, M.D., Southard, R.J., Gruendler, L., 2015. Solfataric alteration  
720 at Hawaii as a potential analog for Martian surface processes. Presented at the AGU Fall  
721 Meeting, San Francisco, CA.

722 Bowen, B.B., Story, S., Oboh-Ikuenobe, F., Benison, K.C., 2013. Differences in regolith  
723 weathering history at an acid and neutral saline lake on the Archean Yilgarn Craton and  
724 implications for acid brine evolution. *Chemical Geology* 356, 126–140.  
725 <https://doi.org/10.1016/j.chemgeo.2013.08.005>

726 Carr, M.H., Head, J.W., 2010. Geologic history of Mars. *Earth and Planetary Science Letters*  
727 294, 185–203. <https://doi.org/10.1016/j.epsl.2009.06.042>

728 Chevrier, V.F., Ulrich, R., Altheide, T.S., 2009. Viscosity of liquid ferric sulfate solutions and  
729 application to the formation of gullies on Mars. *J. Geophys. Res.* 114, E06001.  
730 <https://doi.org/10.1029/2009JE003376>

731 Chojnacki, M., Hynek, B.M., 2008. Geological context of water-altered minerals in Valles  
732 Marineris, Mars. *J. Geophys. Res.* 113, E12005. <https://doi.org/10.1029/2007JE003070>

733 Clark, R., Swayze, G., Wise, R., Livo, K.E., Hoefen, T.M., Kokaly, R.F., Sutley, S.J., 2007. Data  
734 USGS Digital Spectral Library splib06a (Data Series 231), Data Series.

735 Cloutis, E., Hawthorne, F., Mertzman, S., Krenn, K., Craig, M., Marcino, D., Methot, M.,  
736 Strong, J., Mustard, J., Blaney, D., 2006. Detection and discrimination of sulfate minerals

737 using reflectance spectroscopy. *Icarus* 184, 121–157.  
738 <https://doi.org/10.1016/j.icarus.2006.04.003>

739 Crowley, J.K., Williams, D.E., Hammarstrom, J.M., Piatak, N., Chou, I.-M., Mars, J.C., 2003.  
740 Spectral reflectance properties (0.4–2.5  $\mu\text{m}$ ) of secondary Fe-oxide, Fe-hydroxide, and  
741 Fe-sulphate-hydrate minerals associated with sulphide-bearing mine wastes.  
742 *Geochemistry: Exploration, Environment, Analysis* 3, 219–228.  
743 <https://doi.org/10.1144/1467-7873/03-001>

744 Dębniak, K., Mège, D., Gurgurewicz, J., 2017. Geomorphology of Ius Chasma, Valles Marineris,  
745 Mars. *Journal of Maps* 13, 260–269. <https://doi.org/10.1080/17445647.2017.1296790>

746 Dohm, J.M., Tanaka, K.L., 1999. Geology of the Thaumasia region, Mars: plateau development,  
747 valley origins, and magmatic evolution. *Planetary and Space Science* 47, 411–431.  
748 [https://doi.org/10.1016/S0032-0633\(98\)00141-X](https://doi.org/10.1016/S0032-0633(98)00141-X)

749 Flahaut, J., Bishop, J.L., Silvestro, S., Tedesco, D., Daniel, I., Loizeau, D., 2019. The Italian  
750 Solfatara as an analog for Mars fumarolic alteration. *American Mineralogist* 104, 1565–  
751 1577. <https://doi.org/10.2138/am-2019-6899>

752 Flahaut, J., Martinot, M., Bishop, J.L., Davies, G.R., Potts, N.J., 2017. Remote sensing and in  
753 situ mineralogic survey of the Chilean salars: An analog to Mars evaporate deposits?  
754 *Icarus* 282, 152–173. <https://doi.org/10.1016/j.icarus.2016.09.041>

755 Flahaut, J., Quantin, C., Allemand, P., Thomas, P., Le Deit, L., 2010. Identification, distribution  
756 and possible origins of sulfates in Capri Chasma (Mars), inferred from CRISM data. *J.*  
757 *Geophys. Res.* 115, E11007. <https://doi.org/10.1029/2009JE003566>

758 Fueten, F., Flahaut, J., Stesky, R., Hauber, E., Rossi, A.P., 2014. Stratigraphy and mineralogy of  
759 Candor Mensa, West Candor Chasma, Mars: Insights into the geologic history of Valles  
760 Marineris: GEOLOGY OF CANDOR MENSA. *J. Geophys. Res. Planets* 119, 331–354.  
761 <https://doi.org/10.1002/2013JE004557>

762 Fueten, F., Novakovic, N., Stesky, R., Flahaut, J., Hauber, E., Rossi, A.P., 2017. The Evolution  
763 of Juventae Chasma, Valles Marineris, Mars: Progressive Collapse and Sedimentation:  
764 The Evolution of Juventae Chasma. *J. Geophys. Res. Planets* 122, 2223–2249.  
765 <https://doi.org/10.1002/2017JE005334>

766 Gendrin, A., Mangold, N., Bibring, J.-P., Langevin, Y., Gondet, B., Poulet, F., Bonello, G.,  
767 Quantin, C., Mustard, J., Arvidson, R., LeMouélic, S., 2005. Sulfates in Martian Layered  
768 Terrains: The OMEGA/Mars Express View. *Science* 307, 1587–1591.  
769 <https://doi.org/10.1126/science.1109087>

770 Head, J.W., Greeley, R., Golombek, M.P., Hartmann, W.K., Hauber, E., Jaumann, R., Masson,  
771 P., Neukum, G., Nyquist, L.E., Carr, M.H., 2001. Geological Processes and Evolution.  
772 *Space Science Reviews* 96, 263–292. <https://doi.org/10.1023/A:1011953424736>

773 Kaplan, H.H., Milliken, R.E., Fernández-Remolar, D., Amils, R., Robertson, K., Knoll, A.H.,  
774 2016. Orbital evidence for clay and acidic sulfate assemblages on Mars based on  
775 mineralogical analogs from Rio Tinto, Spain. *Icarus* 275, 45–64.  
776 <https://doi.org/10.1016/j.icarus.2016.03.019>

777 Le Deit, L., Flahaut, J., Quantin, C., Hauber, E., Mège, D., Bourgeois, O., Gurgurewicz, J.,  
778 Massé, M., Jaumann, R., 2012. Extensive surface pedogenic alteration of the Martian  
779 Noachian crust suggested by plateau phyllosilicates around Valles Marineris: PLATEAU  
780 PHYLLOSILICATES, MARS. *J. Geophys. Res.* 117, n/a-n/a.  
781 <https://doi.org/10.1029/2011JE003983>

- 782 Lucchitta, B.K., Bertolini, M.L., 1990. Interior structures of Valles Marineris, Mars. Presented at  
783 the Lunar Planet. Sci., XX, pp. 590–591.
- 784 Lucchitta, B.K., Isbell, N.K., Howington-Kraus, A., 1994. Topography of Valles Marineris:  
785 Implications for erosional and structural history. *J. Geophys. Res.* 99, 3783.  
786 <https://doi.org/10.1029/93JE03095>
- 787 Madejová, J., Andrejkovičová, S., Bujdák, J., Čeklovský, A., Hrachová, J., Valúchová, J.,  
788 Komadel, P., 2007. Characterization of products obtained by acid leaching of Fe-  
789 bentonite. *Clay miner.* 42, 527–540. <https://doi.org/10.1180/claymin.2007.042.4.09>
- 790 Madejová, J., Bednarikova, E., Komadel, P., Cicel, B., 1990. Structural study of acid-treated  
791 smectites by IR spectroscopy. Presented at the 11th Conf. on Clay Mineralogy and  
792 Petrology, Budejovice, pp. 267–271.
- 793 Madejová, J., Pentrák, M., Pálková, H., Komadel, P., 2009. Near-infrared spectroscopy: A  
794 powerful tool in studies of acid-treated clay minerals. *Vibrational Spectroscopy* 49, 211–  
795 218. <https://doi.org/10.1016/j.vibspec.2008.08.001>
- 796 McEwen, A.S., Eliason, E.M., Bergstrom, J.W., Bridges, N.T., Hansen, C.J., Delamere, W.A.,  
797 Grant, J.A., Gulick, V.C., Herkenhoff, K.E., Keszthelyi, L., Kirk, R.L., Mellon, M.T.,  
798 Squyres, S.W., Thomas, N., Weitz, C.M., 2007. Mars Reconnaissance Orbiter's High  
799 Resolution Imaging Science Experiment (HiRISE). *J. Geophys. Res.* 112, E05S02.  
800 <https://doi.org/10.1029/2005JE002605>
- 801 Metz, J., Grotzinger, J., Okubo, C., Milliken, R., 2010. Thin-skinned deformation of sedimentary  
802 rocks in Valles Marineris, Mars. *J. Geophys. Res.* 115, E11004.  
803 <https://doi.org/10.1029/2010JE003593>
- 804 Murchie, S.L., Arvidson, R., Bedini, P., Beisser, K., Bibring, J.-P., Bishop, J., Boldt, J.,  
805 Cavender, P., Choo, T., Clancy, R.T., Darlington, E.H., Des Marais, D., Espiritu, R., Fort,  
806 D., Green, R., Guinness, E., Hayes, J., Hash, C., Heffernan, K., Hemmler, J., Heyler, G.,  
807 Humm, D., Hutcheson, J., Izenberg, N., Lee, R., Lees, J., Lohr, D., Malaret, E., Martin,  
808 T., McGovern, J.A., McGuire, P., Morris, R., Mustard, J., Pelkey, S., Rhodes, E.,  
809 Robinson, M., Roush, T., Schaefer, E., Seagrave, G., Seelos, F., Silverglate, P., Slavney,  
810 S., Smith, M., Shyong, W.-J., Strohhahn, K., Taylor, H., Thompson, P., Tossman, B.,  
811 Wirzburger, M., Wolff, M., 2007. Compact Reconnaissance Imaging Spectrometer for  
812 Mars (CRISM) on Mars Reconnaissance Orbiter (MRO). *J. Geophys. Res.* 112, E05S03.  
813 <https://doi.org/10.1029/2006JE002682>
- 814 Murchie, S.L., Mustard, J.F., Ehlmann, B.L., Milliken, R.E., Bishop, J.L., McKeown, N.K., Noe  
815 Dobra, E.Z., Seelos, F.P., Buczkowski, D.L., Wiseman, S.M., Arvidson, R.E., Wray,  
816 J.J., Swayze, G., Clark, R.N., Des Marais, D.J., McEwen, A.S., Bibring, J.-P., 2009a. A  
817 synthesis of Martian aqueous mineralogy after 1 Mars year of observations from the Mars  
818 Reconnaissance Orbiter. *J. Geophys. Res.* 114, E00D06.  
819 <https://doi.org/10.1029/2009JE003342>
- 820 Murchie, S.L., Roach, L., Seelos, F., Milliken, R., Mustard, J., Arvidson, R., Wiseman, S.,  
821 Lichtenberg, K., Andrews-Hanna, J., Bishop, J., Bibring, J.-P., Parente, M., Morris, R.,  
822 2009b. Evidence for the origin of layered deposits in Candor Chasma, Mars, from  
823 mineral composition and hydrologic modeling. *J. Geophys. Res.* 114, E00D05.  
824 <https://doi.org/10.1029/2009JE003343>
- 825 Mustard, J.F., Murchie, S.L., Pelkey, S.M., Ehlmann, B.L., Milliken, R.E., Grant, J.A., Bibring,  
826 J.-P., Poulet, F., Bishop, J., Dobra, E.N., Roach, L., Seelos, F., Arvidson, R.E.,  
827 Wiseman, S., Green, R., Hash, C., Humm, D., Malaret, E., McGovern, J.A., Seelos, K.,

828 Clancy, T., Clark, R., Marais, D.D., Izenberg, N., Knudson, A., Langevin, Y., Martin, T.,  
829 McGuire, P., Morris, R., Robinson, M., Roush, T., Smith, M., Swayze, G., Taylor, H.,  
830 Titus, T., Wolff, M., 2008. Hydrated silicate minerals on Mars observed by the Mars  
831 Reconnaissance Orbiter CRISM instrument. *Nature* 454, 305–309.  
832 <https://doi.org/10.1038/nature07097>

833 Noel, A., Bishop, J.L., Al-Samir, M., Gross, C., Flahaut, J., McGuire, P.C., Weitz, C.M., Seelos,  
834 F., Murchie, S., 2015. Mineralogy, morphology and stratigraphy of the light-toned  
835 interior layered deposits at Juventae Chasma. *Icarus* 251, 315–331.  
836 <https://doi.org/10.1016/j.icarus.2014.09.033>

837 Perrin, S., Bishop, J.L., Parker, W.G., King, S.J., Lafuente, B., 2018. Mars evaporite analog site  
838 containing jarosite and gypsum at Sulfate Hill, Painted Desert, AZ, in: 49th Lunar and  
839 Planetary Science Conference. The Woodlands, TX.

840 Perrin, S.L., Bishop, J.L., Parker, W.G., King, S.J., Lafuente, B., 2018. Mars Evaporite Analog  
841 Site Containing Jarosite and Gypsum at Sulfate Hill, Painted Desert, AZ. Presented at the  
842 49th Annual Lunar and Planetary Science Conference, Woodlands, TX.

843 Roach, L.H., Mustard, J.F., Murchie, S.L., Bibring, J. -P., Forget, F., Lewis, K.W., Aharonson,  
844 O., Vincendon, M., Bishop, J.L., 2009. Testing evidence of recent hydration state change  
845 in sulfates on Mars. *J. Geophys. Res.* 114, E00D02.  
846 <https://doi.org/10.1029/2008JE003245>

847 Roach, L.H., Mustard, J.F., Swayze, G., Milliken, R.E., Bishop, J.L., Murchie, S.L., Lichtenberg,  
848 K., 2010. Hydrated mineral stratigraphy of Ius Chasma, Valles Marineris. *Icarus* 206,  
849 253–268. <https://doi.org/10.1016/j.icarus.2009.09.003>

850 Sánchez-Juny, M., Triadú, A., Andreu, A., Bladé, E., 2019. Hydrodynamic Determination of the  
851 Kinematic Viscosity of Waste Brines. *ACS Omega* 4, 20987–20999.  
852 <https://doi.org/10.1021/acsomega.9b02164>

853 Saranathan, A.M., Parente, M., 2021. Adversarial feature learning for improved mineral mapping  
854 of CRISM data. *Icarus* 355, 114107. <https://doi.org/10.1016/j.icarus.2020.114107>

855 Scott, D.H., Tanaka, K.L., 1986. Geologic map of the western equatorial region of Mars.

856 Seelos, F.P., Seelos, K.D., Murchie, S.L., Novak, M.A.M., Hash, C.D., Morgan, M.F., Arvidson,  
857 R.E., Aiello, J., Bibring, J.-P., Bishop, J.L., Boldt, J.D., Boyd, A.R., Buczkowski, D.L.,  
858 Chen, P.Y., Clancy, R.T., Ehlmann, B.L., Frizzell, K., Hancock, K.M., Hayes, J.R.,  
859 Heffernan, K.J., Humm, D.C., Itoh, Y., Ju, M., Kochte, M.C., Malaret, E., McGovern,  
860 J.A., McGuire, P., Mehta, N.L., Moreland, E.L., Mustard, J.F., Nair, A.H., Núñez, J.I.,  
861 O’Sullivan, J.A., Packer, L.L., Poffenbarger, R.T., Poulet, F., Romeo, G., Santo, A.G.,  
862 Smith, M.D., Stephens, D.C., Toigo, A.D., Viviano, C.E., Wolff, M.J., 2023. The CRISM  
863 investigation in Mars orbit: Overview, history, and delivered data products. *Icarus*  
864 115612. <https://doi.org/10.1016/j.icarus.2023.115612>

865 Sivasankari, T., Arivazhagan, S., 2022. An Analysis of Morphology and Diverse Mineralogy in  
866 Ius Chasma, Valles Marineris Using MCC, CRISM and CTX Data. *J Indian Soc Remote*  
867 *Sens.* <https://doi.org/10.1007/s12524-022-01609-5>

868 Spencer, R.J., 2000. Sulfate Minerals in Evaporite Deposits. *Reviews in Mineralogy and*  
869 *Geochemistry* 40, 173–192. <https://doi.org/10.2138/rmg.2000.40.3>

870 Story, S., Bowen, B.B., Benison, K.C., Schulze, D.G., 2010. Authigenic phyllosilicates in  
871 modern acid saline lake sediments and implications for Mars. *J. Geophys. Res.* 115,  
872 E12012. <https://doi.org/10.1029/2010JE003687>

873 Tanaka, K.L., 1986. The stratigraphy of Mars. *J. Geophys. Res.* 91, E139.  
874 <https://doi.org/10.1029/JB091iB13p0E139>

875 Tanaka, K.L., Golombek, M.P., Banerdt, W.B., 1991. Reconciliation of stress and structural  
876 histories of the Tharsis region of Mars. *J. Geophys. Res.* 96, 15617–15633.  
877 <https://doi.org/10.1029/91JE01194>

878 Thollot, P., Mangold, N., Ansan, V., Le Mouélic, S., Milliken, R.E., Bishop, J.L., Weitz, C.M.,  
879 Roach, L.H., Mustard, J.F., Murchie, S.L., 2012. Most Mars minerals in a nutshell:  
880 Various alteration phases formed in a single environment in Noctis Labyrinthus:  
881 ALTERATION PHASES IN NOCTIS LABYRINTHUS. *J. Geophys. Res.* 117, n/a-n/a.  
882 <https://doi.org/10.1029/2011JE004028>

883 Usabal, G., Bishop, J.L., Danielsen, J.M., Itoh, Y., Parente, M., Seelos, F.P., 2019.  
884 Characterization of Jarosite-Bearing Outcrops Northwest of Mwarth Valles. Presented at  
885 the 50th Lunar Planet. Sci. Conf, The Woodlands, TX.

886 Viviano, C.E., Seelos, F.P., Murchie, S.L., Kahn, E.G., Seelos, K.D., Taylor, H.W., Taylor, K.,  
887 Ehlmann, B.L., Wiseman, S.M., Mustard, J.F., Morgan, M.F., 2014. Revised CRISM  
888 spectral parameters and summary products based on the currently detected mineral  
889 diversity on Mars. *J. Geophys. Res. Planets* 119, 1403–1431.  
890 <https://doi.org/10.1002/2014JE004627>

891 Weitz, C.M., Bishop, J.L., 2016. Stratigraphy and formation of clays, sulfates, and hydrated  
892 silica within a depression in Coprates Catena, Mars: HYDRATED DEPOSITS IN  
893 COPRATES CATENA. *J. Geophys. Res. Planets* 121, 805–835.  
894 <https://doi.org/10.1002/2015JE004954>

895 Weitz, C.M., Bishop, J.L., Thollot, P., Mangold, N., Roach, L.H., 2011. Diverse mineralogies in  
896 two troughs of Noctis Labyrinthus, Mars. *Geology* 39, 899–902.  
897 <https://doi.org/10.1130/G32045.1>

898 Weitz, C.M., Milliken, R.E., Grant, J.A., McEwen, A.S., Williams, R.M.E., Bishop, J.L.,  
899 Thomson, B.J., 2010. Mars Reconnaissance Orbiter observations of light-toned layered  
900 deposits and associated fluvial landforms on the plateaus adjacent to Valles Marineris.  
901 *Icarus* 205, 73–102. <https://doi.org/10.1016/j.icarus.2009.04.017>

902 Weitz, C.M., Noe Dobrea, E., Wray, J.J., 2015. Mixtures of clays and sulfates within deposits in  
903 western Melas Chasma, Mars. *Icarus* 251, 291–314.  
904 <https://doi.org/10.1016/j.icarus.2014.04.009>

905 Weitz, C.M., Noe Dobrea, E.Z., Lane, M.D., Knudson, A.T., 2012. Geologic relationships  
906 between gray hematite, sulfates, and clays in Capri Chasma: GRAY HEMATITE IN  
907 CAPRI CHASMA. *J. Geophys. Res.* 117, n/a-n/a. <https://doi.org/10.1029/2012JE004092>  
908